Chemical Engineering Journal 359 (2019) 1592–1602

Contents lists available at ScienceDirect

Chemical Engineering Journal

journal homepage: www.elsevier.com/locate/cej

Hydrothermal crystallization of $Pmn2_1$ Li_2FeSiO_4 hollow mesocrystals for Li-ion cathode application

Yan Zeng[a], Hsien-Chieh Chiu[a], Majid Rasool[a], Nicolas Brodusch[a], Raynald Gauvin[a], De-Tong Jiang[b], Dominic H. Ryan[c], Karim Zaghib[d], George P. Demopoulos[a,*]

[a] Materials Engineering, McGill University, 3610 rue University, Montréal, QC H3A 0C5, Canada
[b] Department of Physics, University of Guelph, Guelph, ON N1G 2W1, Canada
[c] Department of Physics, McGill University, 3600 rue University, Montréal, QC H3A 2T8, Canada
[d] Centre d'excellence-ETSE, Hydro-Québec, Varennes, QC J3X 1S1, Canada

HIGHLIGHTS

- Novel Li_2FeSiO_4 mesocrystals exhibit improved Li-ion storage properties.
- EDTA-regulated formation of impurity-free and defect-free hollow $Pmn2_1$ crystals.
- Li_2FeSiO_4 mesocrystals form via a 4-step hydrothermal crystallization mechanism.

GRAPHICAL ABSTRACT

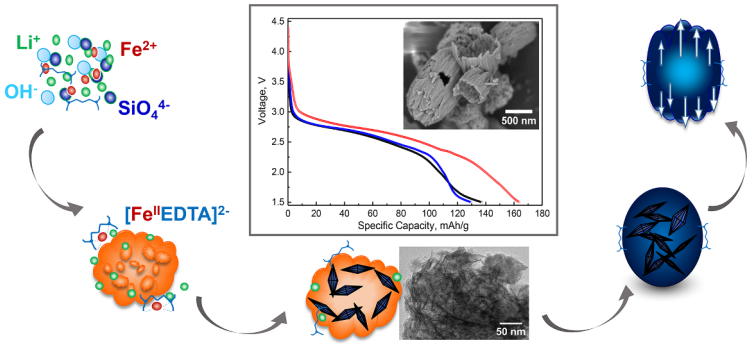

ARTICLE INFO

Keywords:
Li_2FeSiO_4
Hydrothermal synthesis
Concentration effect
EDTA effect
Hollow mesocrystals
Lithium-ion batteries

ABSTRACT

Lithium transition metal orthosilicates such as Li_2FeSiO_4 (LFS) have been recognized as promising cathode materials for application in Li-ion batteries because of their high theoretical energy density, safety, and benign/abundant element composition. Their development, however, has been hampered by the challenge of obtaining phase-pure and defect-free Li_2FeSiO_4 nanoparticles as non-optimized crystal properties have an adverse effect on structural stability and electrochemical performance. Considering the sustainable potential of hydrothermal synthesis in producing electrode materials, here we employ this process to systematically study critical synthesis parameters for optimal control of particle size, morphology, phase purity, and defects of Li_2FeSiO_4 crystallized in the orthorhombic crystal system with space group $Pmn2_1$. It is shown that via a combination of elevated $FeSO_4$ concentration regime and use of EDTA as a complexing agent, phase-pure $Pmn2_1$ particle formation can be controlled. Synchrotron-based XRD Rietveld refinement and ^{57}Fe Mössbauer spectroscopy reveal a significant reduction in Li-Fe antisite defects and presence of Fe^{3+}. Additionally, the use of EDTA promotes the formation of unique peanut-shell looking hollow mesocrystals that are advantageous in maximizing electrode/electrolyte contact resulting in higher Li-ion storage capacity than dense LFS particles. On the basis of detailed XRD, SEM, and TEM characterizations, a four-step crystallization mechanism is proposed to explain the formation of the hollow mesocrystals. These findings bring new insight into our pursuit of optimization of Li_2FeSiO_4 as a cathode material for Li-ion batteries.

* Corresponding author.
E-mail address: george.demopoulos@mcgill.ca (G.P. Demopoulos).

https://doi.org/10.1016/j.cej.2018.11.013
Received 20 July 2018; Received in revised form 31 October 2018; Accepted 2 November 2018
Available online 03 November 2018
1385-8947/

1. Introduction

Developing sustainable and safe cathode materials with high energy and power density is among the primary targets for next-generation rechargeable Li-ion batteries to be used in large-scale stationary energy storage and electric transportation [1–3]. In this context, transition metal orthosilicates Li_2MSiO_4 (M = Fe, Mn, or Co) are receiving increasing attention as cathode materials in view of their high theoretical capacity (~333 mAh/g) arising from the possibility to extract two Li-ions per formula unit [4–7]. Within the silicate family, Li_2FeSiO_4 (LFS) is the most promising one because of its relatively high stability and the abundant non-toxic nature of Fe and Si. Li_2FeSiO_4 is known however to exhibit complex polymorphism, with at least three crystal structures identified, namely one low temperature orthorhombic phase (β_{II}) with space group $Pmn2_1$ [8] and two high temperature phases including a monoclinic phase (γ_s) with space group $P2_1/n$ [9] and an orthorhombic phase (γ_{II}) with space group *Pmnb* [10]. Most of the reported work has focused on the $P2_1/n$ structure either because of its direct formation during high-temperature synthesis processes such as solid-state reaction or due to the phase transformation during the subsequent annealing to achieve carbon coating [11]. However, it has been found that during cycling the $P2_1/n$ phase transforms to a more stable inverse-$Pmn2_1$ phase [12–15]. This cycled inverse-$Pmn2_1$ phase is isostructural with $Pmn2_1$, except that all the Fe have exchanged sites with half of Li. This has therefore prompted our interest in the $Pmn2_1$ phase which can only be produced at temperatures below 500 °C [16].

It is known from a wide range of studies that the morphology and particle size of cathode materials have a direct impact on their electrochemical performance. For example, the formation of $LiFePO_4$ particles of nanometre size or 2D nanoplatelets is considered to enhance electrochemical performance by reducing the Li-ion transport path length [17–20]. In this context, controlling synthesis to produce nanostructured particles suitable for high-performance Li-ion batteries is a critical step in the development of new electrode materials such as Li_2FeSiO_4. Various synthesis methods have been applied to produce Li_2FeSiO_4. While the high-temperature solid-state reaction is the most robust and conventional method, it does not allow for the control of particle size and morphology [8,15,21–23]. The complexity of sol-gel process and the toxic chemicals involved in it may hinder its further application in large-scale production [5,24,25]. In addition, neither the solid-state reaction nor the sol-gel method can produce $Pmn2_1$ Li_2FeSiO_4 because of the high temperatures (600–900 °C) used [11,26]. By comparison, hydrothermal synthesis constitutes a sustainable option to produce nanomaterials with specific properties on a large scale at a reasonable cost and in an environmentally benign manner [27,28]. Several authors have discussed the importance of applying hydrothermal processing to the synthesis of Li-ion battery materials [29–31], including polyanionic compounds such as the silicates and phosphates [32]. Supercritical hydrothermal synthesis conducted at 350–420 °C at a pressure of 38 MPa has been applied to produce LFS nanosheets of the $Pmn2_1$ polymorph [33], but the method does not lend itself to large-scale application.

To date, a number of studies on the hydrothermal preparation of Li_2FeSiO_4 have appeared [34–38]. However, the formation of phase-pure Li_2FeSiO_4 is relatively difficult to achieve during hydrothermal synthesis due to undesirable side reactions, which lead to hydrolytic co-precipitation of impurity phases like Li_2SiO_3, Fe_3O_4, Fe_2O_3, and FeOOH [36–38]. Such impurities are also encountered in solvothermal synthesis, where ethylene glycol–water solution instead of pure water is used [39–41]. Solvothermal synthesis can produce Li_2FeSiO_4 particles with hierarchical morphologies but long reaction time from 4 to 8 days is required for the completion of crystallization. Even when phase-pure Li_2FeSiO_4 is obtained, as reported by Sirisopanaporn et al., intersite exchange between Li and Fe occurs, resulting in undesirable defects as was the case of $Pmn2_1$ phase hydrothermally synthesized at 200 °C [34–35]. The occurrence of such antisite defects has been widely investigated in the case of $LiFePO_4$ in terms of their impact on Li-ion diffusion and electrochemical performance [17,42]. Luckily, in the case of $LiFePO_4$ or the high-temperature monoclinic ($P2_1/n$) form of Li_2FeSiO_4, these antisite defects are removed effectively during subsequent annealing at ~700 °C. This approach cannot however be applied to the low-temperature orthorhombic ($Pmn2_1$) Li_2FeSiO_4 phase as it is not stable at high temperatures.

With the overriding goal of producing defect-free $Pmn2_1$ Li_2FeSiO_4 to evaluate its electrochemical performance as intercalation cathode, herein we report a systematic study on the hydrothermal synthesis of this material. Synthesis parameters including temperature, reaction time, precursor concentration, and the addition of EDTA as complexing agent are investigated. The hydrothermal treatment leads to reactive crystallization of LFS in the form of mesocrystals via oriented nanocrystallite assembly [43], whilst the presence of EDTA allows the formation of a unique hollow structure. The formation mechanism is investigated by taking samples during hydrothermal operation. Synchrotron-based XRD with Rietveld refinement and Mössbauer spectroscopy have allowed for quantification of Li-Fe antisite defects and Fe^{3+} as an impurity enabling the synthesis of phase-pure and defect-free LFS with promising charge and discharge characteristics.

2. Experimental section

2.1. Synthesis

Lithium iron silicate (Li_2FeSiO_4, LFS) was prepared by hydrothermal synthesis from starting materials of lithium hydroxide monohydrate (98% LiOH H_2O), fumed silica (99% SiO_2), iron(II) sulfate heptahydrate (98% $FeSO_4$ $7H_2O$), ascorbic acid (99% $C_6H_8O_6$), and ethylenediaminetetraacetic acid calcium disodium salt (99% EDTA-Ca-2Na). All the chemicals were purchased from Sigma-Aldrich.

In a typical synthesis, SiO_2 powder was dissolved in 160 mL of LiOH aqueous solution in an ultrasonic bath for 1.5 h. Then 40 mL of $FeSO_4$ solution was added dropwise with a peristaltic pump to the LiOH/SiO_2 solution in a N_2-filled glovebox to avoid oxidation of the ferrous iron. The molar ratio of Li:Fe:Si was kept at 4:1:1 for all syntheses. Ascorbic acid (AA) with the molar ratio AA:Fe = 0.16:1 was added as a reducing agent to further prevent ferrous iron oxidation. The concentration of Li^+ was varied from 0.4 to 1.6 M in the mixed precursor solution and the obtained LFS product powders were denoted as LFS04M, LFS08M, LFS12M, and LFS16M, correspondingly. EDTA was used with all other conditions being the same as in LFS08M. The molar ratio of EDTA:Fe was 0.16:1 and the product was denoted as LFSEDTA. Hydrothermal synthesis was performed in a 450 mL Teflon-lined stirred autoclave (Parr Instruments, Moline, IL) at different temperatures (up to 200 °C) for variable times (0–12 h) and stirring speed of 300 rpm. The stirring feature allows for uniform distributions of reactants and products. Moreover, the autoclave is equipped with a dip tube, which permits sampling during the hydrothermal operation [44]. A Parr 4848 reactor controller was used to allow for continuous control and monitoring of temperature and pressure. After completion of hydrothermal precipitation, the autoclave was cooled down to room temperature within 30 min. The obtained slurry was separated in a centrifuge. The wet solids were rinsed twice with deoxygenate deionized water (again to avoid undesirable oxidation of ferrous iron) and once with acetone, followed by drying in a vacuum oven at 80 °C for 12 h. The dried powders were stored in a glovebox to minimize exposure to oxygen and moisture.

For the investigation of the particle formation mechanism, slurry samples were collected from the dip tube during the heat-up period at various times/temperatures, namely at 100 °C (after 20 min), 120 °C (after 30 min), 160 °C (after 40 min), and 200 °C (after 50 min, which is the end of the heating ramp). To avoid oxidation of ferrous iron, a custom-made container filled with argon gas was used to collect the slurry products and was transferred to a glovebox immediately. Dried

powder for subsequent characterizations or electrochemical evaluation was obtained after centrifugation, washing with deoxygenated/deionized water, and drying in a vacuum oven at 80 °C for 12 h.

2.2. Material characterization

Synchrotron X-ray diffraction (XRD) measurements were taken at the Hard X-ray Micro-Analysis (HXMA) beamline at Canadian Light Source (CLS). The wavelength of the X-ray was λ = 0.6889 Å. A mar345 image plate detector was used to record the Debye-Scherrer rings from thin pellet samples made from the pristine powders. Calibration was done by using the synchrotron XRD pattern of LaB_6 powder sample. Laboratory XRD was performed on a Bruker D8-Advantage powder diffractometer using Co-Kα radiation (λ = 1.78892 Å, 35 kV; 15 mA) from 2θ = 10 to 100° in a step of 0.02°. Rietveld refinement was done using TOPAS Academic V.5.0 program.

A Hitachi SU-8230 cold-field emission scanning electron microscope (CFE-SEM) (Hitachi High Technologies) was employed for particle morphology characterization. Transmission electron microscope (TEM) and high-resolution TEM (HR-TEM) images were acquired in an FEI Tecnai 12 BioTwin TEM at 200 kV. Brunauer–Emmett–Teller (BET) specific surface area measurements were performed using a TriStar 3000 analyzer (Micromeritics) in N_2 (−196 °C). Inductively coupled plasma optical emission spectroscopy (ICP-OES, Thermo Scientific iCAP 6500 ICP spectrometer) was applied for elemental analysis. Prior to ICP measurements, LFS powders were digested by using mixed concentrated acid HCl:HF (3:1 vol%) at 95 °C for 3 h, followed by dilution with 4 vol% HNO_3.

^{57}Fe transmission Mössbauer spectroscopy was collected in an in-house facility in a constant acceleration mode at room temperature with ^{57}Co Rh source. 0.03 g of LFS powders were used for each measurement. Velocity calibration and isomer shifts (IS) were quoted with respect to α-iron foil. Parameter fittings were performed using a standard least-squares minimisation with Lorentzian lines.

2.3. Electrochemistry

The pristine powder products were mixed with acetylene black (AB) in a weight ratio of 0.8:0.2 and ball milled at 250 rpm for 3 h using planetary micro mill (Fritsch, Pulverisette 7 premium line). 100 g of 1 mm ZrO_2 grinding balls were used for per 1 g of LFS-AB mixture in 15 mL of isopropanol. This procedure enables mechanical carbon coating and simultaneous nanosizing of the LFS particles while preserving the low-T orthorhombic phase ($Pmn2_1$). The working electrodes were prepared by spreading a slurry of the active material (ball-milled C-LFS), acetylene black, and poly(vinylidenedifluoride) (PVDF) in a weight ratio of (C-LFS:AB:PVDF) 0.8:0.1:0.1 onto aluminum foil. Metallic lithium was used as the counter electrode. A polypropylene film (Celgard 2200) was used as the separator. Each final electrode contained approximately 2.5 mg/cm^2 of active Li_2FeSiO_4 material. A standard electrolyte solution made of 1 M $LiPF_6$/ethylene carbonate (EC)/dimethyl carbonate (DMC) (1:1 by volume) was used. The data of the galvanostatic charge and discharge profile was collected on an 8-Channel Battery Analyzer (MTI Corporation, USA). The charge and discharge cycling were performed at C/50 rate (1C = 166 mAh/g) in the voltage range of 1.5–4.5 V at 55 °C. Electrochemical Impedance Spectroscopy (EIS) measurements performed on electrodes before cycling (after a 6-hour relaxation period) were carried out on an electrochemical workstation (Bio-Logic) in potentiostatic mode between 1 MHz and 20 mHz at open circuit voltage (OCV). The resistances are determined by fitting the Nyquist plot with the Equivalent Electric Circuit by Z-fit method provided by EC-Lab software.

3. Results and discussion

3.1. Reactive crystallization of Li_2FeSiO_4

To investigate the hydrothermal formation mechanism of crystalline Li_2FeSiO_4 particles, slurry products were collected during the heating up of the pressure reactor from room temperature to the target temperature (200 °C) and characterized by synchrotron XRD, SEM, TEM, and ICP techniques. Fig. 1 shows the evolution of XRD patterns of precipitates collected from solution with 0.8 M LiOH at different reaction time and temperature. In the beginning (i.e. before heating starts), the drop-wise addition of $FeSO_4$ aqueous solution to the $LiOH/SiO_2$ solution (pH = 11.8) resulted in spontaneous formation of a colloidal white suspension, which gradually changed to a pale green color at the final pH = 11.2 of the mixed solution. This spontaneous reaction can be attributed to forced hydrolysis of iron(II) representing the formation of $Fe(OH)_2$ colloids [45]. After washing and drying, the collected precursor powder, denoted as LFSRT, was characterized by synchrotron XRD (Fig. 1). As shown in the bottom pattern in Fig. 1, one broad XRD band at around 2θ = 15.5° was observed. When using a laboratory Co source XRD instrument over a wider 2θ range, two broad XRD bands were observed (Fig. S1). Elemental analysis using ICP (Fig. S2) shows that this precursor precipitate contains a Li to Fe mole ratio of 0.43:1 and a Si to Fe ratio of 0.74:1. ICP analysis of the filtrate confirms that all the Fe (less than 2×10^{-5} mol/L in filtrate) had precipitated, whereas the respective amounts for Si and Li were 81.5% and 17.5%. On the basis of this analysis it is proposed that the spontaneously formed hydrolytic precipitate (LFSRT) consists mainly of poorly crystalline ferrous hydroxide along with the adsorbed or co-precipitated silicate and lithium species (possibly as one or more of silica, ferrous silicate, and lithium silicate) as commonly observed in multi-ion hydrolytic precipitation systems [46,47].

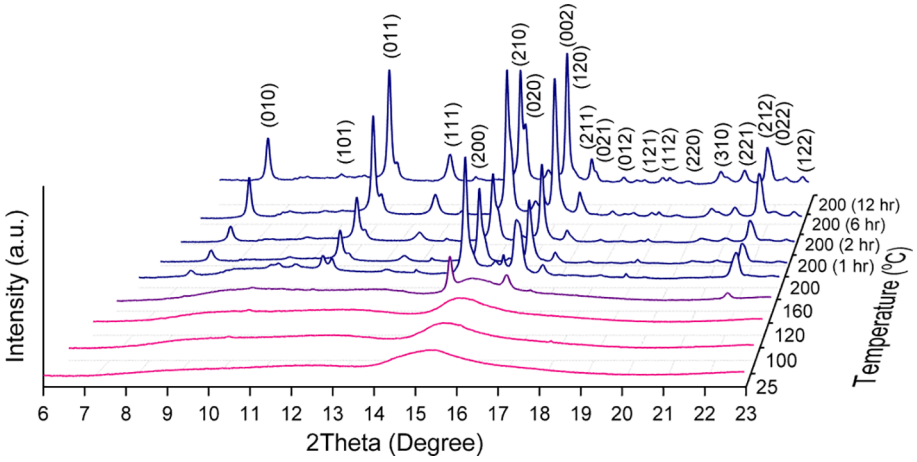

Fig. 1. Synchrotron XRD (λ = 0.6889 Å) patterns of hydrothermal precipitates obtained at different temperatures and times from 25 to 200 °C (heat-up period) and held at 200 °C for (1, 2, 6, and 12) hours. Bragg peak positions correspond to $Pmn2_1$ Li_2FeSiO_4 (reference PDF# 01-080-6279).

Following the precursor precipitation in the glove box, the slurry was transferred to an autoclave and heated up to 200 °C in 50 min, during which products were collected and characterized. As can be seen from Fig. 1 (but also Fig. S1), the powders obtained at 100 and 120 °C, denoted as LFS100C and LFS120C, respectively, have broad XRD features similar to the room temperature precursor precipitate, LFSRT. ICP analysis of the solids (Fig. S2) shows that the Li to Fe mole ratio was still around 0.4–0.45:1, whereas the Si to Fe mole ratio increased to 1:1 as the reaction temperature increased to 100 and 120 °C. The concentrations of Fe and Si in the solution were insignificant, indicating that all of the Fe and Si had precipitated out.

The first signs of nucleation-crystallization of Li_2FeSiO_4 appear after 40 min when the temperature has reached 160 °C (LFS160C) as revealed in Fig. 1. More specifically, three diffraction peaks emerge at $2\theta = 14.6^\circ$, 16.1° and 21.8° corresponding to the (2 1 0), (0 0 2) and (0 2 2) facets, respectively, of *Pmn*2$_1$ Li_2FeSiO_4 [35]. It should be noted however that the diffraction peaks is rather weak reflecting the early stages of nucleation of a nanocrystalline phase. In addition, the coexistence of the broad background featureindicates that not all the precursor precipitate has been rearranged into a crystalline structure. Ten minutes later with the temperature reaching 200 °C (LFS200C), we can see crystallization has accelerated as now all the diffraction peaks of *Pmn*2$_1$ LFS appear and their intensities have increased. These results indicate that the crystallization of LFS is not progressing through homogeneous nucleation but rather through the precipitation of a poorly crystalline ferrous hydroxide/silicate intermediate that undergoes solution-mediated heterogeneous transformation upon heating into crystalline LFS. The crystallinity of LFS can be seen (in Fig. 1) to improve as the holding time at 200 °C is extended to 1, 2, and 6 h as evidenced by the increased peak intensity. No further improvement is observed when the hydrothermal time at 200 °C is extended to 12 h. The XRD pattern of Li_2FeSiO_4 synthesized at 200 °C for 6 h (denoted as LFS08M) is very well indexed as the *Pmn*2$_1$ LFS [35]. Rietveld refinement of the XRD data will be discussed in a later section.

We further confirmed the reactive crystallization mechanism of LFS by identifying the evolution of morphology and crystal structure. Fig. S3 shows low-magnification features of the reaction intermediates from the precursor precipitate (LFSRT) to one-hour hydrothermally treated product (LFS200C1H). It reveals that before reaching 200 °C, the precipitated particles have irregular size and shape. Clearly, conversion occurred when the temperature reached 200 °C as we can see that the precipitates are dominantly smaller round-shape particles. After holding at 200 °C for 1 h, the chunk-like particles have almost disappeared, and the precipitate is composed of dispersed uniform round-shaped particles. These morphological analyses, combined with the XRD results, provide a clue that a critical conversion of the amorphous intermediate to crystalline LFS happened right before 200 °C.

For further confirmation and understanding of the conversion process, high-magnification SEM and high-resolution TEM were performed on LFS160C (40 min heat-up), LFS200C (50 min heat-up), and LFS08M (6 h holding time). Fig. 2a shows the surface morphology of LFS160C, revealing that the freshly nucleated nanocrystalline LFS is in the form of aggregates of smaller 100–150 nm (primary) particles. Higher magnification SEM image (Fig. 2b) reveals the LFS160C having a honeycomb-like nanoarchitecture. With further observation through TEM (Fig. 2c) and HR-TEM (Fig. 2d), the nanoparticles are seen to be made of sub-nm thick nanocrystalline fibers interweaved together. BET specific surface area of LFS160C is 111.16 m^2/g, approximately ten-fold greater than that of the final LFS product. This extremely high surface area can be attributed to the 2-D nanofiber features of LFS160C.

As the temperature increased to 200 °C (LFS200C), elliptical bulk particles form (Fig. 2e) via the evolution of LFS160C. These (primary) particles are now about 1 μm in diameter and have very rough surface (Fig. 2f). TEM and HR-TEM images (Fig. 2g, h) of LFS200C show that the primary particles are made of assemblies of smaller irregular shape components with the characteristic crystalline fiber nanostructure that have been bonded together apparently via secondary nucleation. Additionally, the BET surface area was found to drop dramatically to 6–8 m^2/g, further confirming the transformation of 2-D nanofibers to 3-D crystalline particles.

SEM images of LFS08M (LFS obtained after 6 h hydrothermal processing at 200 °C) reveal that the as-synthesized fully crystalline primary particles are elliptical (or barrel-like) in shape with size about 800 nm in waist diameter and 1.2 μm in length (Fig. 2i, j). The barrel-

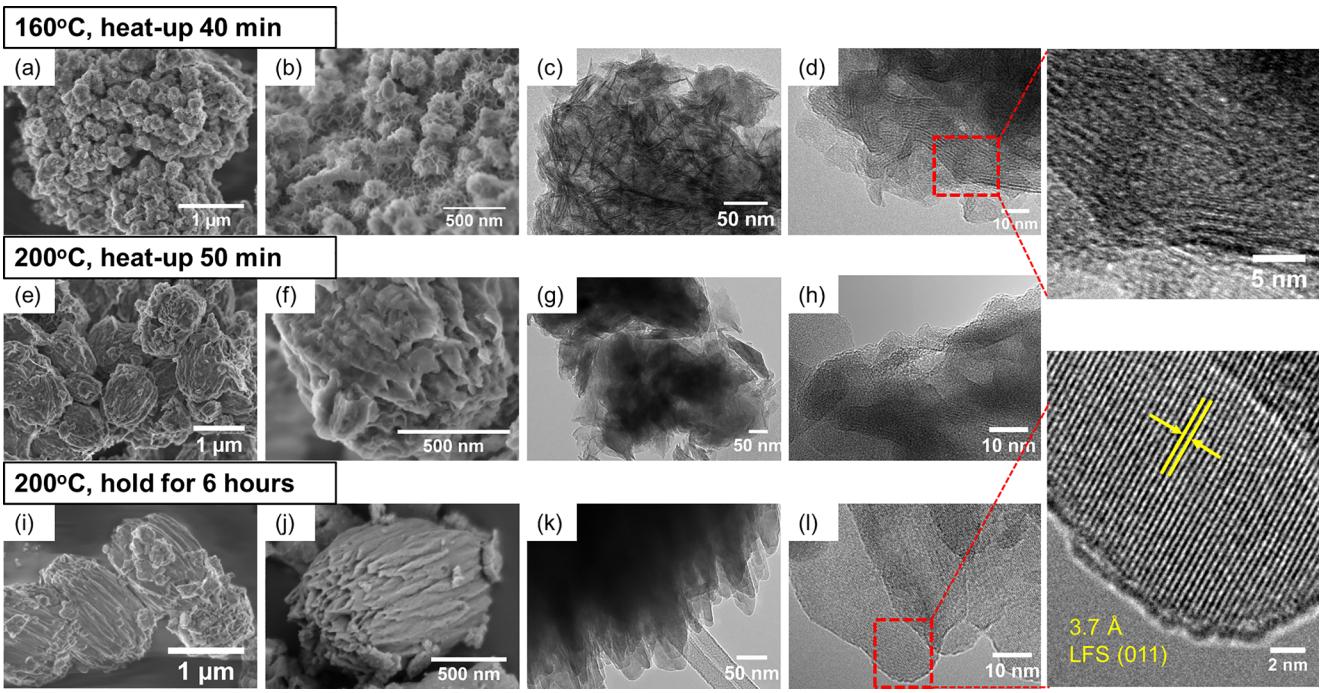

Fig. 2. SEM, TEM, and HR-TEM images of hydrothermal precipitates obtained either during heat-up period at (a–d) 160 °C (LFS160C, 40 min) and at (e–h) 200 °C (LFS200C, 50 min); and (i–l) at 200 °C after 6 h (LFS08M).

like shape is built from elongated nanocrystals with width ranging from 20 to 50 nm, as can be seen in Fig. 2k. HR-TEM image of the edge of an LFS08M particle (Fig. 2l) reveals that the nanocrystals have high crystallinity and all the adjacent nanocrystals are assembled in the same crystallographic orientation. This special feature is characteristic of mesocrystals, a rather unique class of crystalline materials made up via alignment of nanocrystals along the same crystallographic order over a microscopic scale [43]. The lattice fringe shown in the HR-TEM image has a d-spacing of 3.7 Å, which corresponds to the (0 1 1) plane of LFS. Analysis of the synchrotron XRD by Rietveld refinement indicates that the crystallite size of LFS08M is 45.4(6) nm.

3.2. Effect of precursor concentration

In the attempt to control the morphology and size of LFS particles via supersaturation adjustment, a series of experiments at different precursor concentrations were conducted. The reaction time was kept at 6 h, the temperature at 200 °C, and the molar ratio of Li:Fe:Si at 4:1:1, i.e. Fe and Si were at the stoichiometric ratio and Li at 100% excess. Yabuuchi et al. found that 100% excess of Li is required for the synthesis of LFS under hydrothermal treatment [48]. Four Li^+ concentrations were examined, namely 0.4, 0.8, 1.2, and 1.6 M, and the samples are denoted as LFS04M, LFS08M, LFS12M, and LFS16M, respectively. Fig. 3 shows the XRD patterns of the as-synthesized products. All the four products can be indexed to the $Pmn2_1$ LFS. Interestingly fewer peaks (labeled with a *) denoting the presence of minor iron oxide impurities are found in the products obtained at the high range of precursor concentrations. By far the LFS04M product obtained with 0.4 M Li^+ was found to be the least pure.

Concentration determines the supersaturation of the crystallization system which ultimately controls the kinetics of particle nucleation and growth [49]. Particle morphological characteristics as a function of precursor concentrations are presented in Fig. 4. It can be seen that LFS04M and LFS08M have similar shape and particle size-about 1200 nm long and 600 nm diameter (Fig. 4a, b). BET specific areas of LFS04M and LFS08M are 7.22 and 8.66 m^2/g, respectively. Nitrogen adsorption–desorption isotherms associated with the BET analysis can be found in the Supplementary Data (Fig. S4). However, when the starting concentration of Li^+ was increased to 1.2 M, the particle size of LFS decreased significantly to ~ 200 nm in diameter and ~ 400 nm in length (Fig. 4c) and the BET specific surface area increased to 26.05 m^2/g, which is almost 3× of the magnitude of the lower concentration LFS products. No further change in particle size (Fig. 4d) and surface area (27.16 m^2/g) was observed when the precursor Li concentration was raised from 1.2 to 1.6 M. TEM images of LFS08M and LFS16M are compared in Fig. 4e and f. Similar to LFS08M, LFS16M particles are assembled by oriented attachment of elongated nanocrystals, although the size of the nanocrystals is smaller than those assembled in LFS08M.

3.3. Effect of EDTA complexing additive

The purity and morphology of the hydrothermally synthesized LFS crystals were further optimized when EDTA was added into the reaction mixture as a complexing agent. The XRD data of the EDTA-produced LFS (denoted as LFSEDTA) is analyzed and discussed in terms of crystal structure and purity in the next Section 3.4. Here we describe the crystal morphological effects of EDTA. As the SEM images in Fig. 5a,b indicates that the ellipsoidal LFSEDTA were formed from many elongated crystals looking similar to LFS08M in terms of their exterior. The particle size is about 1 μm in length and 500 nm in diameter. Remarkably, some of the particles were broken in half revealing a unique hollow structure resembling with peanut shell. As a result, the BET surface area of LFSEDTA increased to 11.70 m^2/g, higher than that of LFS08M (i.e. 8.66 m^2/g). Fig. 5c (TEM) clearly illustrates the hollow structure which can be seen from the contrast between the inner sphere and the outer shell. In HR-TEM images, d-spacings of 3.7 Å, 4.1 Å (Fig. 5d, e), and 5.3 Å (Fig. 5f, g) can be observed, which correspond to the (0 1 1), (1 1 0), and (0 1 0) facets, respectively, of $Pmn2_1$ LFS. Hollow nanostructured materials hold a lot of promise as Li-ion storage electrode materials as they allow for intimate interfacing with the electrolyte phase while their thin shell walls provide short diffusion length for larger Li-ion storage capacities provoking the interest of a number of studies. Some notable examples in this regard are the preparation of nanoporous γ-MnO_2 and nano-cage $NiCo_2O_4$ as anode materials [50,51], hollow-structured Co_3O_4 nanoparticles and the study of their capacity fade [52], the synthesis of hollow nanospheres of Li_2CoSiO_4/C as cathode material [53], and the nanoengineering of some unique hollow nanoboxes of Li_2MnSiO_4@C as high capacity cathode [54]. Typically, however, synthesis of hollow particles is accomplished via template-based or other complex multi-step methods that are not amenable to scale up. The only attempt to produce hollow Li_2FeSiO_4 particles has been reported by Xu et al. [39]. The authors produced their hollow LFS particles in mixed solvent media (1/3 ethylene glycol-2/3 water) after 3-days hydrothermal reaction that were further sintered at 650 °C for 10 h to promote their C-coating that resulted in obtaining the monoclinic ($P2_1$) phase. Questions are raised if their hollow spherical particles had not densified due to sintering upon annealing as no detailed data were presented. Notwithstanding this issue, we do not as yet have a study that reports template-free or organic solvent-free hydrothermal synthesis of hollow nanostructured LFS particles crystallized in the $Pmn2_1$ system as done here. The mechanism of EDTA-mediated formation of the hollow (peanut-shell like) LFS particles is discussed at a later section.

3.4. Rietveld refinement and Mössbauer spectroscopy

Rietveld refinement of the synchrotron XRD data was applied to extract crystal structure information of three LFS products, namely LFSEDTA, LFS08M, and LFS16M. Fig. 6a–c shows comparisons between observed and fitted patterns of LFSEDTA, LFS08M, and LFS16M with R_{wp} values of 3.821%, 5.429%, and 3.821%, respectively. The starting atomic coordinates are taken from Sirisopanaporn et al. [35]. Only the orthorhombic crystalline Li_2FeSiO_4 phase with space group $Pmn2_1$ was found to fit the data. The minor iron oxide impurities observed in some samples were not taken into account for the refinement. The extracted

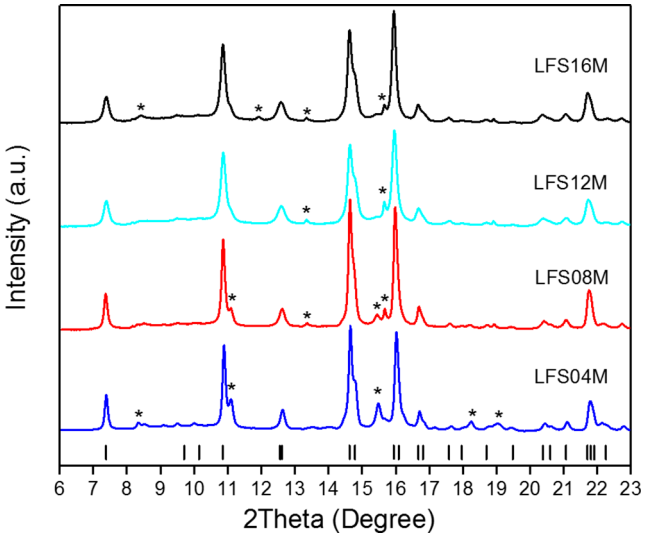

Fig. 3. Synchrotron XRD (λ = 0.6889 Å) patterns of LFS prepared from precursor solution containing Li^+ concentration of 0.4, 0.8, 1.2, and 1.6 M, denoted as LFS04M, LFS08M, LFS12M, and LFS16M, respectively. Black streaks at the bottom represent the Bragg peak positions of $Pmn2_1$ Li_2FeSiO_4 (reference PDF# 01-080-6279). Star symbols shown represent iron (hydr)oxide impurities.

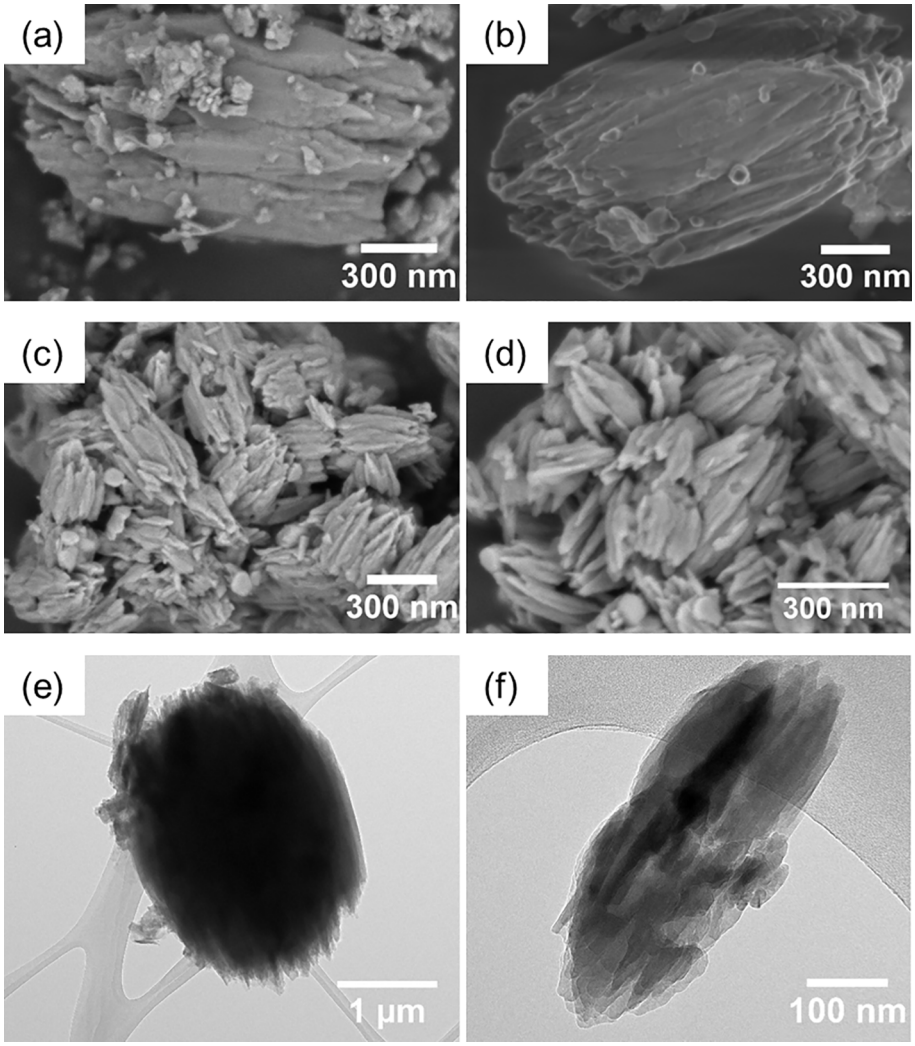

Fig. 4. SEM images of LFS prepared from precursor solutions containing Li^+ concentration of (a) 0.4 M, (b) 0.8 M, (c) 1.2 M, and (d) 1.6 M, denoted as LFS04M, LFS08M, LFS12M, and LFS16M, respectively. TEM images of (e) LFS08M and (f) LFS16M.

unit cell parameters of LFSEDTA are $a = 6.26451(16)$ Å, $b = 5.34467(15)$ Å, and $c = 4.96216(8)$ Å, which agree well with the reported results for *Pmn*2_1 structure [35,55]. During refinement, Fe and Li were allowed to occupy on each other's site and it was assumed that each site is fully occupied. Table S1 lists the atomic fractional coordinates and site occupancies of LFSMEDTA.

In the ideal *Pmn*2_1 structure of Li_2FeSiO_4, Li and Fe atoms occupy different crystallographic sites, denoted as Li1 (4b site) and Fe1 (2a site), respectively. During electrochemical lithiation/delithiation, Li migrates in either a straight *a*-direction or a zig-zag *c*-direction according to DFT computational studies as illustrated in Fig. S5a [12,56]. However, intersite exchange of Li and M has been reported in orthosilicates Li_2MSiO_4 (M = Fe, Mn, or Co) and identified as the most energetically favourable defect in atomistic simulations of Li_2MnSiO_4 [57,58]. In a recent study of post-mortem synchrotron-based XRD and XANES characterizations on monoclinic and orthorhombic phases of Li_2FeSiO_4, Lu et al. demonstrated that Li-Fe antisite defects can be induced during cycling and play an important role in the phase transformation [14]. Sirisopanaporn et al. [35] observed that 5% of the Li1 site was occupied by Fe and 10% of the Fe1 site was occupied by Li in the *Pmn*2_1 Li_2FeSiO_4 that was hydrothermally synthesized at 200 °C using 0.4 M starting Li concentration. After electrochemical cycling, all the Fe will exchange sites with half of the Li, leading to an inverse-*Pmn*2_1 structure [12,13]. In the inverse-*Pmn*2_1 LFS, Li may migrate in a zig-zag *c*-direction or a zig-zag *b*-direction (Fig. S5b) [12,56]. However, if there are local Fe/Li antisite defects, resulting in a non-established *b*-direction channel, the nearby Li-ions could be blocked (see Fig. S5c). Hence to address this concern, it should be beneficial to minimize the formation of antisite defects during synthesis.

According to the present Rietveld refinement analysis, all three as-synthesized LFS materials (Fig. 6) were also found to have certain Li-Fe antisite defects. The concentration of Fe antisite defect (Fe on Li1 site) is of particular interest as it may block the Li diffusion pathway during electrochemical cycling and thereby degrade the performance of the cell. Thus, as depicted in Fig. 7 (detailed data is listed in Table S2), the Fe antisite defect (atom%) was determined to be 3.6%, 10.1%, and 8.9%, respectively, for LFSEDTA, LFS08M, and LFS16M. Li occupancy on Fe1 site (Li antisite defect) was found to be 11.5%, 20.8%, and 30.3%, respectively, for LFSEDTA, LFS08M, and LFS16M. However, it is difficult to acquire a totally accurate refinement for Li antisite defects with only XRD data because Li atoms are weakly scattered by X-rays. One possible origin of the rather high concentrations of Li antisite defects could be the difficulty to differentiate a vacancy from a Li-occupancy. Simultaneous analysis with X-ray and neutron diffraction would make the analysis of Li-occupancy more accurate. Nevertheless, there is clear indication that tuning the synthesis conditions can reduce the formation of Li-Fe antisite defects in LFS. Recently, Paolella *et al.* studied the formation of antisite defects of $LiFePO_4$ during hydrothermal synthesis and found that the addition of Ca^{2+} helped to alter the crystallization path, leading to substantial reduction of antisite defects

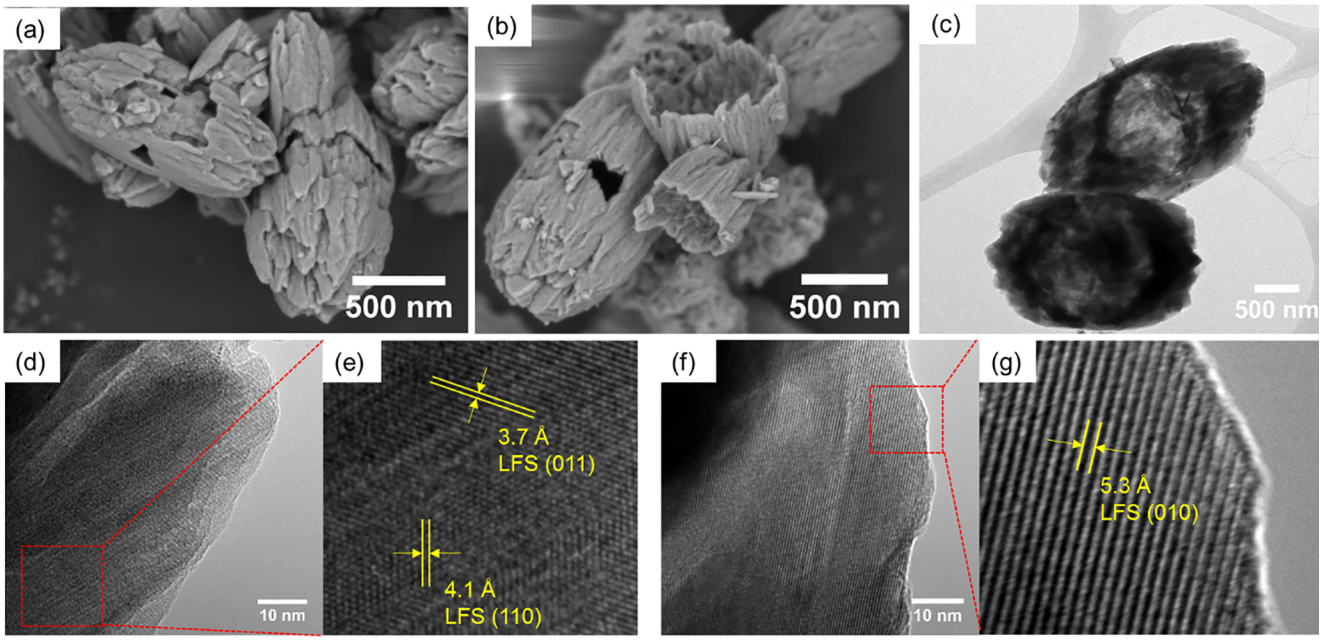

Fig. 5. Morphology and crystal structure of LFSEDTA particles. (a, b) SEM images. (c) TEM image. (d, e) HR-TEM image and its larger magnification showing two d-spacings, 3.7 Å and 4.1 Å, corresponding to the (0 1 1) and (1 1 0) facets, respectively, of *Pmn*2$_1$ Li_2FeSiO_4. (f, g) HR-TEM image and its larger magnification showing a d-spacing of 5.3 Å, corresponding to the (0 1 0) facet of *Pmn*2$_1$ Li_2FeSiO_4.

[17]. In this work, the use of EDTA as an additive has proven to be an effective alternative strategy to reduce the occurrence of antisite defects during hydrothermal synthesis without contaminating the final nanostructured cathode material.

^{57}Fe Mössbauer spectroscopy was applied to further demonstrate the beneficial effects of EDTA on the properties of the hydrothermally prepared LFS products. Fig. 8 shows the Mössbauer spectra obtained from three LFS samples. The parameters extracted from Mössbauer spectra include isomer shift (IS, mm/s), quadrupole splitting (QS, mm/s), and intensities (atom%). These results are tabulated in Table S3. The overall shape of the spectra suggests a dominant Fe^{2+} component (solid green lines) and a minor Fe^{3+} component (dash blue lines). The IS values of Fe^{2+} in the three products range from 0.959(3) to 0.991(1) mm/s, which are typical for Fe^{2+} in tetrahedral coordination with oxygen. For Fe^{3+} doublets, IS values range from 0.28(2) to 0.330(8) mm/s, whereas QS is in the range of 0.69(1) to 0.85(5) mm/s, which are the indication of Fe^{3+} in the environment of iron-oxygen tetrahedra [23,55]. From the area ratios of the Fe^{2+} and Fe^{3+} absorption doublets, Mössbauer results indicate that the LFS produced in the absence of EDTA contain a significant amount of Fe^{3+} ranging from 29.9% to 37.5% in LFS08M and LFS16M, respectively. The Fe^{3+} content is remarkably lower in LFSEDTA, only 7.7%.

The existence of Fe^{3+} in the LFS has been reported in many studies involving different synthesis methods such as via hydrothermal [55,59], solvothermal [41], solid-state [23], or sol-gel [60]. Dominko et al. reported 19.2% of Fe^{3+} in the LFS sample synthesized at 150 °C for 14 days [59]. Liivat et al. [61] observed 22% and Yang et al. [41] even found 45.5% Fe^{3+} in the fresh electrodes. It is possible that some Fe^{3+} came from the oxidation of nanocrystalline LFS after synthesis during handling despite the caution taken as described in the Experimental part [62]. During Mössbauer measurement, the powder was exposed to the air which could also cause the oxidation of Fe^{2+} on the material surface. It is suggested that during future Mössbauer measurements of air-sensitive materials such as LFS, a special air-free sample holder should be used. It should be noted that the relative intensity of the two doublets not only depends on the atomic fraction of these two Fe components, but also their recoil-free factor, *f*. So far, the fitting procedure of relative ratio of Fe^{2+} and Fe^{3+} has been always made on the assumption that they have the same recoil-free factor, which could lead to an overestimation or underestimation of the Fe^{3+} concentration as pointed out by Mysen [63].

As discussed above, the limitation of current characterization techniques could lead to an overestimation of the antisite defects and Fe^{3+} components. Nevertheless, the relative defect concentrations of LFSEDTA, LFS08M, and LFS16M are still valid. Fig. 7 demonstrates that the relative antisite defects amount follows the trend of Fe^{3+} concentration with LFSEDTA having the least amount of antisite defects and Fe^{3+}. The detailed data can be found in Table S2.

3.5. Formation mechanism of LFS mesocrystals

A 4-step mechanism as illustrated in Fig. 9 is proposed to account for the formation of LFS mesocrystals by hydrothermal crystallization. Mesocrystals is a special class of crystalline materials with highly ordered nanoparticle superstructure formed via aligned assembly of nanocrystallites [43]. They have only the last ten years that have been identified and described [43]. Their unique particle morphology gives them interesting physical, chemical, and electrochemical properties as candidate materials for energy storage application [43,64,65]. The underlying mesocrystal formation mechanism was determined via sampling and analysis of intermediates as function of hydrothermal reaction progress. The role that EDTA plays in regulating the crystallization of defect-free LFS mesocrystals with hollow structure is elaborated.

Step 1): In the beginning, spontaneous nucleation and aggregation occur to form a hydrolytic precipitate containing mainly ferrous hydroxides along with adsorbed or co-precipitated silicate and lithium species (Fig. S3). These metastable solid phases form as intermediates because the barriers for their nucleation are smaller than that for the more stable phases. In the presence of EDTA, however, Fe^{2+} is partially chelated forming soluble $[Fe^{II}(EDTA)]^{2-}$ complex. The formation constant of $[Fe^{II}(EDTA)]^{2-}$ at 25 °C is $\log K_f = 14.32$ [66]. The complexation of Fe species alters the reactivity of Fe^{2+} hence modifying the LFS crystallization pathway.

Step 2): As the temperature and pressure increase during

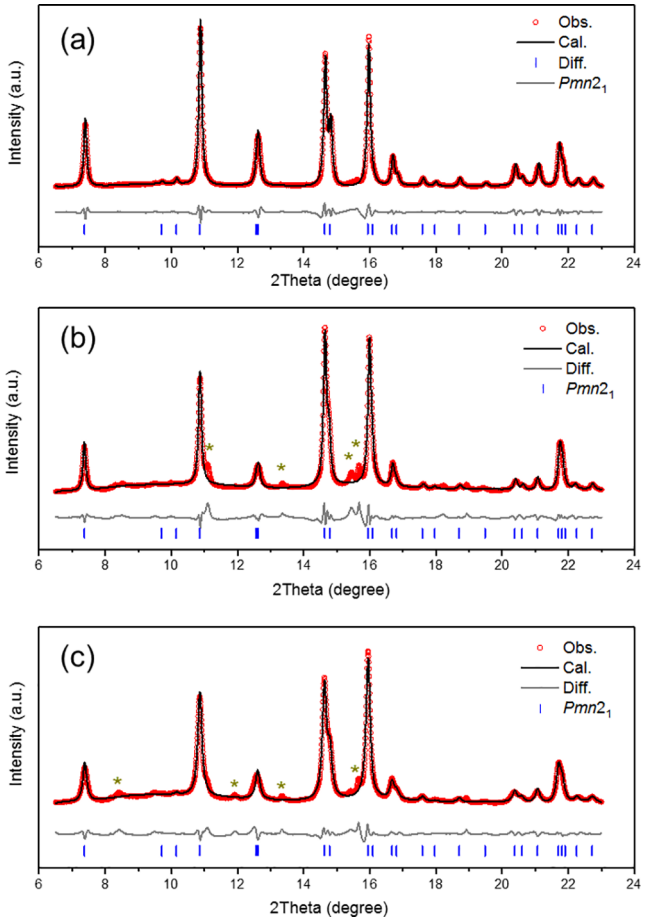

Fig. 6. Rietveld refinement of synchrotron XRD (λ = 0.6889 Å) patterns of Li_2FeSiO_4 products of (a) LFSEDTA; (b) LFS08M; and (c) LFS16M. Red open symbols represent the experimental observation, black curve is the calculation results, grey curve is the difference between observation and calculation, and blue streaks at the bottom represent the Bragg peak positions of *Pmn*2$_1$ Li_2FeSiO_4. Star symbols shown in (b) and (c) represent iron (hydr)oxide impurities. (For interpretation of the references to colour in this figure legend, the reader is referred to the web version of this article.)

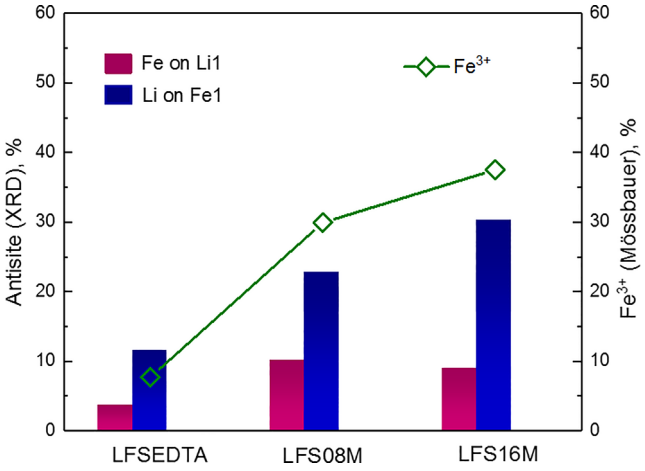

Fig. 7. Percent antisite defect concentrations determined by Rietveld refinement and percent Fe^{3+} contents determined from Mössbauer spectra for LFSEDTA, LFS08M, and LFS16M.

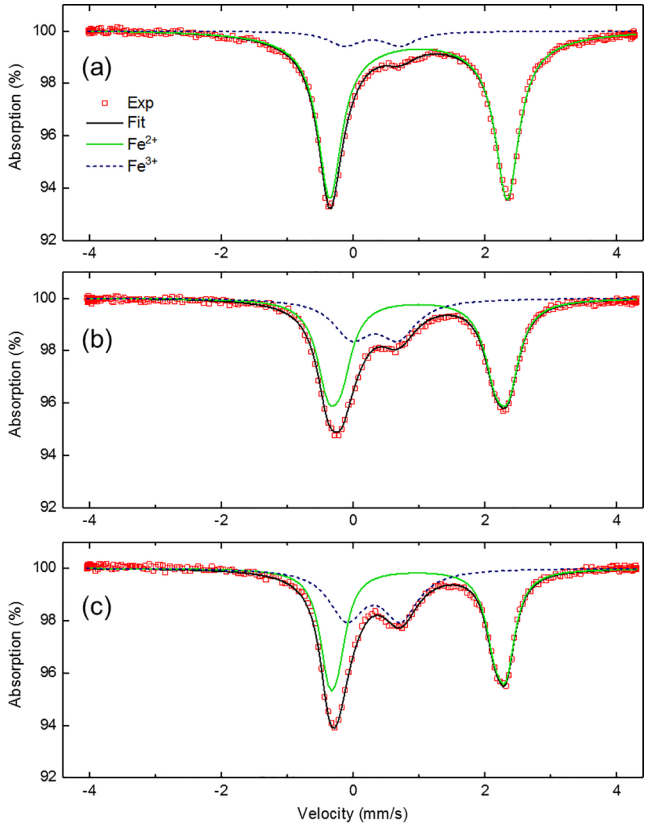

Fig. 8. ^{57}Fe Mössbauer spectra of (a) LFSEDTA; (b) LFS08M; and (c) LFS16M. Red symbols are data measured from the experiment, black lines stand for the overall fitting results, while solid green and dash blue lines represent Fe^{2+} and Fe^{3+} components respectively. (For interpretation of the references to colour in this figure legend, the reader is referred to the web version of this article.)

hydrothermal treatment, heterogeneous nucleation of the more stable crystalline phase (i.e. LFS) takes place from the metastable intermediate solid species through local dissolution and recrystallization (refer to Fig. 2a–d). During this stage, more Li ions are supplied from the solution to complete the formation of stoichiometric LFS, as evidenced by ICP elemental analysis (Fig. S2). The phase transformation from metastable to more stable phases can be referred to as the Stranski's or Ostwald step rule which states that more often the thermodynamically unstable phases occur first, followed by the thermodynamically stable phases [49,67]. Simultaneously, the $[Fe^{II}(EDTA)]^{2-}$ complex undergoes hydrothermal decomposition at elevated temperature and releases Fe^{2+} [68,69]. Thus unlike the system where EDTA is absent, the Fe^{2+} cations that are required for the crystallization of LFS are provided not only by the *in situ* dissolution of iron hydroxide but also by the dissociation of the $[Fe^{II}(EDTA)]^{2-}$ complex. The regulation of the Fe^{2+} concentration in the solution can control the supersaturation of the LFS crystallization. In consequence, the product LFSEDTA has the lowest occurrence of defects including Li-Fe antisite defects and oxidized iron species Fe^{3+}.

Step 3): The newly formed non-bulk nanoparticles of LFS act as building blocks and attach to each other through nearly-oriented attachment to produce larger mesocrystals, releasing the surface energies associated with their free surfaces (Fig. 2e–h) [70]. This step can be considered as the initial growth stage of LFS.

Step 4): The initially formed mesocrystals are not in a fully crystalline state. With further time progression, according to the Ostwald ripening process [71], the particles in the center have lower crystallinity than the outside and thus prefer to dissolve, thereby promoting the growth of outer shell which has higher crystal stability. As we can see by comparing the morphology of LFS08M (Fig. 4c) with that of LFSEDTA (Fig. 5e), the hollow structure is formed only in the presence of EDTA. This suggests that beyond

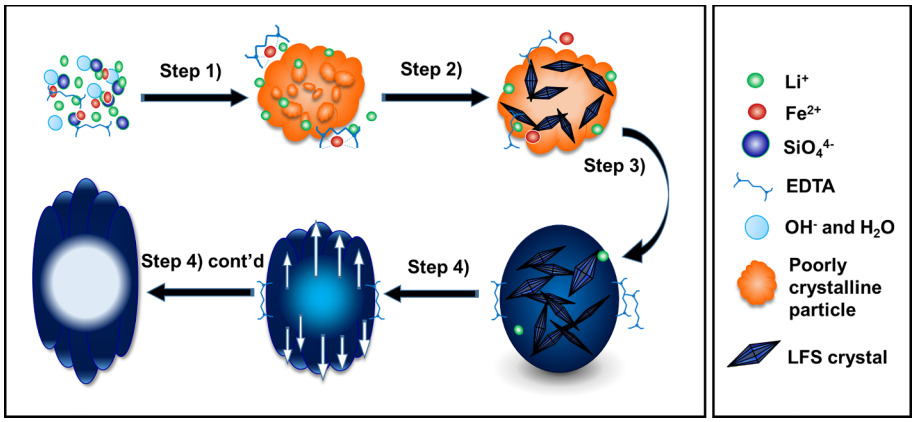

Fig. 9. Proposed scheme for the crystallization of LFS in EDTA-mediated hydrothermal system. Step 1): nucleation and aggregation of poorly crystalline intermediates; Step 2): crystallization of LFS non-bulk 2D nanocrystals out from the intermediates; Step 3): nearly-oriented attachment to assemble bulk LFS mesocrystals; Step 4): dissolution of inner particles and growth of the outer shell into peanut shell-like hollow mesocrystals.

regulating the crystal structure, EDTA also plays a role in modifying the crystal growth pattern of LFS. It has been reported that EDTA can bind to a specific surface of magnetite during its hydrothermal synthesis resulting in dodecahedral nanocrystals [72]. Hollow microspheres of $BiVO_4$ were synthesized through microwave hydrothermal method by manipulating the chelating effect of EDTA with Bi^{3+} [73]. For the growth of LFS, it is reasonable to suspect that EDTA may bind to a preferred crystal surface thus facilitating the growth of the 2D nanocrystals. The controlled release of Fe^{2+} may also contribute to the hollow structure. Consequently, ellipsoidal peanut-shell-like hollow mesocrystals are formed (Fig. 2i–l and Fig. 5).

3.6. Electrochemical performance

The hydrothermally synthesized pristine powders were examined as cathode materials by performing galvanostatic charge and discharge tests. All of the measurements were carried out at C/50 rate in the voltage range of 1.5–4.5 V (vs. Li/Li^+) at 55 °C. The first discharge and the second charge curves are shown in Fig. 10a. Charging and discharging capacities up to 6 cycles can be found in Fig. S6. LFSEDTA exhibited an initial discharge capacity of 164 mAh/g, which is 98.6% of the theoretical capacity (166 mAh/g, assuming that one Li^+ is intercalated into the structure). This capacity is superior to previously reported values measured under similar conditions (e.g. current rate and temperature) on $Pmn2_1$ LFS materials [36,59,74] that have not been submitted to annealing [36] or coating with conductive materials [74]. This is attributed to the well-controlled crystallization process enabling the unique hollow and defect-free mesocrystal structure. Here we may remark that in some previous studies, Li_2FeSiO_4 with $P2_1/n$ crystal structure has been shown to deliver enhanced initial capacity corresponding to the extraction of more than one Li^+ per formula unit [75–77]. It remains unclear, however, whether this extra capacity is a result of the redox reactions of Fe^{3+}/Fe^{4+} and/or O^{2-}/O^- or can be at least partly attributed to the electrolyte degradation [15,61,77,78]. The latter cannot be excluded because typically all the studies that achieved capacity beyond 166 mAh/g were conducted at a rather high voltage cut-off, *ca.* 4.8 V. In this study, we applied a relatively safe voltage range, i.e. 1.5–4.5 V, focusing only on the extraction-insertion of the first Li^+.

In comparison, the EDTA-free synthesized LFS materials, LFS08M and LFS16M, exhibited lower discharge capacities than LFSEDTA in the first cycle, which were 137 and 130 mAh/g (82.6% and 78.2% of the theoretical capacity), respectively. It is proposed that the absence of impurities, but more importantly the lower amount of antisite defects and the hollow structure of the LFSEDTA particles are responsible for the superior performance vis-à-vis the LFS08M and LFS16M materials. Moreover, LFSEDTA shows a higher area below the discharge curve (more plateau-like shape), which denotes a higher energy density compared with the other two products. It is noted however that upon cycling (Fig. S6), the capacity of LFSEDTA decreased to 146 mAh/g, close to that of LFS08M. To probe the origin of the initial enhanced performance exhibited by the hollow LFSEDTA mesocrystals vis-à-vis the LFS08M mesocrystals the two pristine electrodes were subjected to

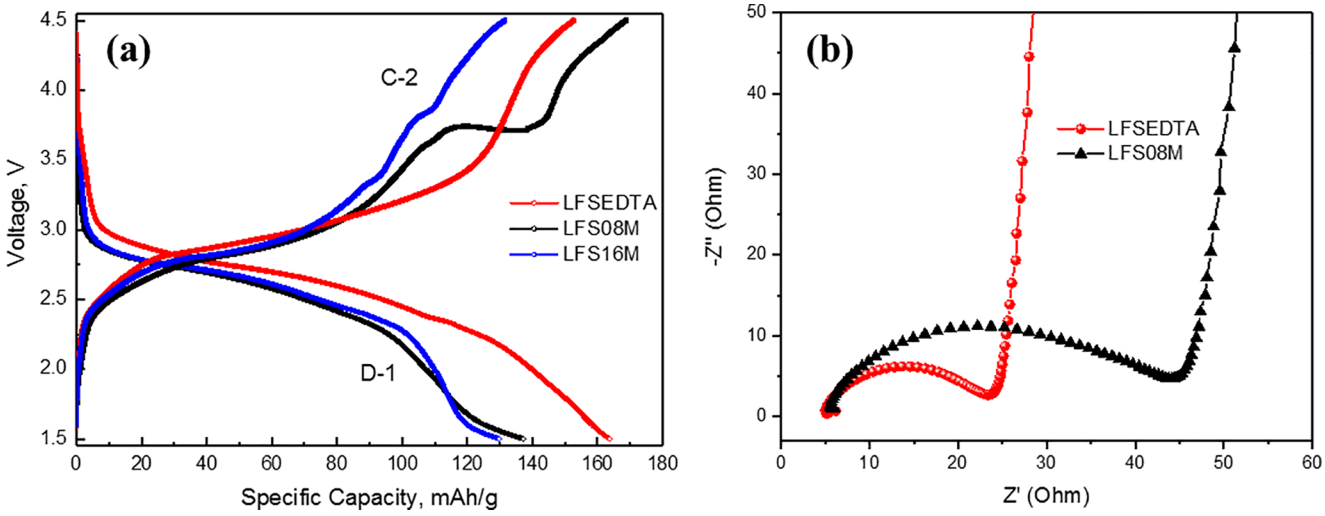

Fig. 10. (a) Galvanostatic curves of the first discharge and the second charge cycles of LFSEDTA, LFS08M, and LFS16M at C/50 rate in the voltage range of 1.5–4.5 V at 55 °C. (b) Electrochemical impedance spectroscopy (EIS) of pristine LFSEDTA and LFS08M electrodes.

EIS analysis. As it can be seen in Fig. 10b, the EDTA-controlled mesocrystals revealed a lower charge-transfer resistance as evidenced by the relative size of the semicircle in the high-to-middle frequency range that represents R_s and R_{ct}, the interface resistance and charge-transfer resistance, respectively. While LFSEDTA is found to have $R_s = 17.9\,\Omega$ and $R_{ct} = 2.3\,\Omega$, LFS08M has higher values of both resistances with $R_s = 25.5\,\Omega$ and $R_{ct} = 12.3\,\Omega$. Having developed the new crystallization process, attention will be shifted next to surface modification to fully exploit the potential of $Pmn2_1$ LFS mesocrystals as higher energy density cathode materials.

4. Conclusions

With the systematic study on the hydrothermal synthesis of Li_2FeSiO_4, we were able to control the size, purity, and defect concentration in $Pmn2_1$ orthorhombic phase particles characterized by unique mesocrystal morphology. By increasing the precursor concentration, crystallization favored the production of smaller nanoparticles with a higher surface area. Rietveld refinement of synchrotron XRD data was used to examine the effects of precursor concentration and EDTA additive on the Li-Fe antisite defects concentrations. Fe oxidation states were analysed by ^{57}Fe Mössbauer spectroscopy. The application of EDTA as a complexing agent allowed for effective control of LFS crystallization process enabling the production of high purity mesocrystals with a unique hollow structure and minimized the occurrence of defect formation and Fe^{2+} oxidation. As a result, the EDTA-assisted synthesized LFS material exhibited superior initial discharge capacity of nearly one-Li storage (164 mAh/g) owing to reduced interfacial charge transfer resistance as confirmed by EIS. The formation mechanism of LFS mesocrystals under EDTA-mediated hydrothermal conditions was proposed to involve four steps: 1) spontaneous precipitation of metastable intermediate phases, 2) local dissolution and transformation of intermediate phases to stable LFS phase, 3) initial growth by nearly-oriented attachment of nanocrystallites into mesocrystals, and 4) further growth to form hollow structure by Ostwald ripening.

Acknowledgments

This work is funded by a Hydro-Québec/Natural Sciences & Engineering Research Council of Canada (NSERC) Collaborative R&D research grant (463484-2014). YZ and GPD acknowledge additional support by the McGill Engineering Doctoral Award (MEDA) and McGill Sustainability Systems Initiative (MSSI) programs. Synchrotron radiation measurements were performed at the Canadian Light Source (CLS), which is supported by CFI, NSERC, University of Saskatchewan, Province of Saskatchewan, Western Economic Diversification Canada, NRC Canada, and CIHR.

Appendix A. Supplementary data

Supplementary data to this article can be found online at https://doi.org/10.1016/j.cej.2018.11.013.

References

[1] M. Armand, J.M. Tarascon, Building better batteries, Nature 451 (7179) (2008) 652–657.
[2] B. Dunn, H. Kamath, J.-M. Tarascon, Electrical energy storage for the grid: a battery of choices, Science 334 (6058) (2011) 928–935.
[3] J.W. Choi, D. Aurbach, Promise and reality of post-lithium-ion batteries with high energy densities, Nat. Rev. Mater. 1 (2016) 16013.
[4] M.E. Arroyo-de Dompablo, M. Armand, J.M. Tarascon, U. Amador, On-demand design of polyoxianionic cathode materials based on electronegativity correlations: an exploration of the Li_2MSiO_4 system (M = Fe, Mn Co, Ni), Electrochem. Commun. 8 (8) (2006) 1292–1298.
[5] R. Dominko, M. Bele, M. Gaberšček, A. Meden, M. Remškar, J. Jamnik, Structure and electrochemical performance of Li_2MnSiO_4 and Li_2FeSiO_4 as potential Li-battery cathode materials, Electrochem. Commun. 8 (2) (2006) 217–222.
[6] R. Dominko, Li_2MSiO_4 (M = Fe and/or Mn) cathode materials, J. Power Sources 184 (2) (2008) 462–468.
[7] M.S. Islam, R. Dominko, C. Masquelier, C. Sirisopanaporn, A.R. Armstrong, P.G. Bruce, Silicate cathodes for lithium batteries: alternatives to phosphates? J. Mater. Chem. 21 (27) (2011) 9811–9818.
[8] A. Nytén, A. Abouimrane, M. Armand, T. Gustafsson, J.O. Thomas, Electrochemical performance of Li_2FeSiO_4 as a new Li-battery cathode material, Electrochem. Commun. 7 (2) (2005) 156–160.
[9] S.-I. Nishimura, S. Hayase, R. Kanno, M. Yashima, N. Nakayama, A. Yamada, Structure of Li_2FeSiO_4, J. Am. Chem. Soc. 130 (40) (2008) 13212–13213.
[10] A. Boulineau, C. Sirisopanaporn, R. Dominko, A.R. Armstrong, P.G. Bruce, C. Masquelier, Polymorphism and structural defects in Li_2FeSiO_4, Dalton Trans. 39 (27) (2010) 6310–6316.
[11] H.N. Girish, G.Q. Shao, Advances in high-capacity Li_2MSiO_4 (M = Mn, Fe Co, Ni,) cathode materials for lithium-ion batteries, RSC Adv. 5 (119) (2015) 98666–98686.
[12] A.R. Armstrong, N. Kuganathan, M.S. Islam, P.G. Bruce, Structure and lithium transport pathways in Li_2FeSiO_4 cathodes for lithium batteries, J. Am. Chem. Soc. 133 (33) (2011) 13031–13035.
[13] C. Eames, A.R. Armstrong, P.G. Bruce, M.S. Islam, Insights into changes in voltage and structure of Li_2FeSiO_4 polymorphs for lithium-ion batteries, Chem. Mater. 24 (11) (2012) 2155–2161.
[14] X. Lu, H.-C. Chiu, Z. Arthur, J. Zhou, J. Wang, N. Chen, D.-T. Jiang, K. Zaghib, G.P. Demopoulos, Li-ion storage dynamics in metastable nanostructured Li_2FeSiO_4 cathode: antisite-induced phase transition and lattice oxygen participation, J. Power Sources 329 (2016) 355–363.
[15] T. Masese, C. Tassel, Y. Orikasa, Y. Koyama, H. Arai, N. Hayashi, J. Kim, T. Mori, K. Yamamoto, Y. Kobayashi, H. Kageyama, Z. Ogumi, Y. Uchimoto, Crystal structural changes and charge compensation mechanism during two lithium extraction/insertion between Li_2FeSiO_4 and $FeSiO_4$, J. Phys. Chem. C 119 (19) (2015) 10206–10211.
[16] A.R. Armstrong, C. Sirisopanaporn, P. Adamson, J. Billaud, R. Dominko, C. Masquelier, P.G. Bruce, Polymorphism in Li_2MSiO_4 (M = Fe, Mn): a variable temperature diffraction study, Z. Anorg. Allg. Chem. 640 (6) (2014) 1043–1049.
[17] A. Paolella, S. Turner, G. Bertoni, P. Hovington, R. Flacau, C. Boyer, Z. Feng, M. Colombo, S. Marras, M. Prato, L. Manna, A. Guerfi, G.P. Demopoulos, M. Armand, K. Zaghib, Accelerated removal of Fe-antisite defects while nanosizing hydrothermal $LiFePO_4$ with Ca^{2+}, Nano Lett. 16 (4) (2016) 2692–2697.
[18] C. Delacourt, P. Poizot, S. Levasseur, C. Masquelier, Size effects on carbon-free $LiFePO_4$ powders: the key to superior energy density, Electrochem. Solid-State Lett. 9 (7) (2006) A352–A355.
[19] M. Gaberscek, R. Dominko, J. Jamnik, Is small particle size more important than carbon coating? An example study on $LiFePO_4$ cathodes, Electrochem. Commun. 9 (12) (2007) 2778–2783.
[20] A. Örnek, Positive effects of a particular type of microwave-assisted methodology on the electrochemical properties of olivine $LiMPO_4$ (M = Fe, Co and Ni) cathode materials, Chem. Eng. J. 331 (2018) 501–509.
[21] D. Jugović, M. Milović, V.N. Ivanovski, M. Avdeev, R. Dominko, B. Jokić, D. Uskoković, Structural study of monoclinic Li_2FeSiO_4 by X-ray diffraction and Mössbauer spectroscopy, J. Power Sources 265 (2014) 75–80.
[22] K. Zaghib, A. Ait Salah, N. Ravet, A. Mauger, F. Gendron, C.M. Julien, Structural, magnetic and electrochemical properties of lithium iron orthosilicate, J. Power Sources 160 (2) (2006) 1381–1386.
[23] A. Nytén, S. Kamali, L. Häggström, T. Gustafsson, J.O. Thomas, The lithium extraction/insertion mechanism in Li_2FeSiO_4, J. Mater. Chem. 16 (23) (2006) 2266–2272.
[24] A. Kumar, O.D. Jayakumar, V.M. Naik, G.A. Nazri, R. Naik, Improved electrochemical properties of solvothermally synthesized Li_2FeSiO_4/C nanocomposites: a comparison between solvothermal and sol-gel methods, Solid State Ionics 294 (2016) 15–20.
[25] M. Bini, S. Ferrari, C. Ferrara, M.C. Mozzati, D. Capsoni, A.J. Pell, G. Pintacuda, P. Canton, P. Mustarelli, Polymorphism and magnetic properties of Li_2MSiO_4 (M = Fe, Mn) cathode materials, Sci. Rep. 3 (2013) 03452.
[26] S. Sun, C. Matei Ghimbeu, C. Vix-Guterl, M.-T. Sougrati, C. Masquelier, R. Janot, Synthesis of Li_2FeSiO_4/carbon nano-composites by impregnation method, J. Power Sources 284 (2015) 574–581.
[27] K. Byrappa, T. Adschiri, Hydrothermal technology for nanotechnology, Prog. Cryst. Growth Charact. Mater. 53 (2) (2007) 117–166.
[28] M. Yoshimura, K. Byrappa, Hydrothermal processing of materials: past, present and future, J. Mater. Sci. 43 (7) (2008) 2085–2103.
[29] J. Chen, A review of nanostructured lithium ion battery materials via low temperature synthesis, Recent Patent Nanotechnol. 7 (1) (2013) 2–12.
[30] J. Chen, S. Wang, M.S. Whittingham, Hydrothermal synthesis of cathode materials, J. Power Sources 174 (2) (2007) 442–448.
[31] M.K. Devaraju, I. Honma, Hydrothermal and solvothermal process towards development of $LiMPO_4$ (M = Fe, Mn) nanomaterials for lithium-ion batteries, Adv. Energy Mater. 2 (3) (2012) 284–297.
[32] C. Masquelier, L. Croguennec, Polyanionic (phosphates, silicates, sulfates) frameworks as electrode materials for rechargeable Li (or Na) batteries, Chem. Rev. 113 (8) (2013) 6552–6591.
[33] D. Rangappa, K.D. Murukanahally, T. Tomai, A. Unemoto, I. Honma, Ultrathin nanosheets of Li_2MSiO_4 (M = Fe, Mn) as High-Capacity Li-Ion battery electrode, Nano Lett. 12 (3) (2012) 1146–1151.
[34] C. Sirisopanaporn, R. Dominko, C. Masquelier, A.R. Armstrong, G. Mali, P.G. Bruce, Polymorphism in $Li_2(Fe, Mn)SiO_4$: a combined diffraction and NMR study, J. Mater. Chem. 21 (44) (2011) 17823–17831.

[35] C. Sirisopanaporn, C. Masquelier, P.G. Bruce, A.R. Armstrong, R. Dominko, Dependence of Li_2FeSiO_4 electrochemistry on structure, J. Am. Chem. Soc. 133 (5) (2011) 1263–1265.

[36] N. Yabuuchi, Y. Yamakawa, K. Yoshii, S. Komaba, Low-temperature phase of Li_2FeSiO_4: crystal structure and a preliminary study of electrochemical behavior, Dalton Trans. 40 (9) (2011) 1846–1848.

[37] H. Kageyama, Y. Hashimoto, Y. Oaki, H. Imai, Six-armed twin crystals composed of lithium iron silicate nanoplates and their electrochemical properties, CrystEngComm 17 (44) (2015) 8486–8491.

[38] Y. Xu, W. Shen, C. Wang, A. Zhang, Q. Xu, H. Liu, Y. Wang, Y. Xia, Hydrothermal synthesis and electrochemical performance of nanoparticle Li_2FeSiO_4/C cathode materials for lithium ion batteries, Electrochim. Acta 167 (2015) 340–347.

[39] Y. Xu, W. Shen, A. Zhang, H. Liu, Z. Ma, Template-free hydrothermal synthesis of Li_2FeSiO_4 hollow spheres as cathode materials for lithium-ion batteries, J. Mater. Chem. A 2 (32) (2014) 12982–12990.

[40] J. Yang, X. Kang, D. He, T. Peng, L. Hu, S. Mu, Hierarchical shuttle-like Li_2FeSiO_4 as a highly efficient cathode material for lithium-ion batteries, J. Power Sources 242 (2013) 171–178.

[41] J. Yang, X. Kang, D. He, A. Zheng, M. Pan, S. Mu, Graphene activated 3D-hierarchical flower-like Li_2FeSiO_4 for high-performance lithium-ion batteries, J. Mater. Chem. A 3 (32) (2015) 16567–16573.

[42] K. Zaghib, A. Guerfi, P. Hovington, A. Vijh, M. Trudeau, A. Mauger, J.B. Goodenough, C.M. Julien, Review and analysis of nanostructured olivine-based lithium rechargeable batteries: status and trends, J. Power Sources 232 (2013) 357–369.

[43] E.V. Sturm, H. Cölfen, Mesocrystals: structural and morphogenetic aspects, Chem. Soc. Rev. 45 (21) (2016) 5821–5833.

[44] K. Vediappan, A. Guerfi, V. Gariépy, G.P. Demopoulos, P. Hovington, J. Trottier, A. Mauger, K. Zaghib, C.M. Julien, Effect of the stirring during the hydrothermal synthesis of C-LiFePO$_4$, ECS Trans. 58 (14) (2014) 67–72.

[45] E.R. Encina, M. Distaso, R.N. Klupp Taylor, W. Peukert, Synthesis of goethite α-FeOOH particles by air oxidation of ferrous hydroxide $Fe(OH)_2$ suspensions: insight on the formation mechanism, Cryst. Growth Des. 15 (1) (2015) 194–203.

[46] X. Meng, S. Bang, G.P. Korfiatis, Effects of silicate, sulfate, and carbonate on arsenic removal by ferric chloride, Water Res. 34 (4) (2000) 1255–1261.

[47] D.A. Dzombak, M.F. Morel, Surface Complexation Modeling: Hydrous Ferric Oxide, Wiley, New York, 1990.

[48] N. Yabuuchi, Y. Yamakawa, K. Yoshii, S. Komaba, Hydrothermal synthesis and characterization of Li_2FeSiO_4 as positive electrode materials for Li-ion batteries, Electrochemistry 78 (5) (2010) 363–366.

[49] G.P. Demopoulos, Aqueous precipitation and crystallization for the production of particulate solids with desired properties, Hydrometallurgy 96 (3) (2009) 199–214.

[50] J. Zhao, Z. Tao, J. Liang, J. Chen, Facile synthesis of nanoporous γ-MnO_2 structures and their application in rechargeable Li-ion batteries, Cryst. Growth Des. 8 (8) (2008) 2799–2805.

[51] X. Hou, S. Xue, M. Liu, X. Shang, Y. Fu, D. He, Hollow irregular octahedra-like $NiCo_2O_4$ cages composed of mesoporous nanosheets as a superior anode material for lithium-ion batteries, Chem. Eng. J. 350 (2018) 29–36.

[52] Y. Kim, J.-H. Lee, S. Cho, Y. Kwon, I. In, J. Lee, N.-H. You, E. Reichmanis, H. Ko, K.-T. Lee, H.-K. Kwon, D.-H. Ko, H. Yang, B. Park, Additive-free hollow-structured Co_3O_4 nanoparticle Li-ion battery: the origins of irreversible capacity loss, ACS Nano 8 (7) (2014) 6701–6712.

[53] G. He, G. Popov, L.F. Nazar, Hydrothermal synthesis and electrochemical properties of Li_2CoSiO_4/C nanospheres, Chem. Mater. 25 (7) (2013) 1024–1031.

[54] X.-F. Yang, J.-H. Yang, K. Zaghib, M.L. Trudeau, J.Y. Ying, Synthesis of phase-pure Li_2MnSiO_4@C porous nanoboxes for high-capacity Li-ion battery cathodes, Nano Energy 12 (2015) 305–313.

[55] G. Mali, C. Sirisopanaporn, C. Masquelier, D. Hanzel, R. Dominko, Li_2FeSiO_4 polymorphs probed by Li-6 MAS NMR and Fe-57 Mössbauer spectroscopy, Chem. Mater. 23 (11) (2011) 2735–2744.

[56] A. Liivat, J.O. Thomas, Li-ion migration in Li_2FeSiO_4-related cathode materials: a DFT study, Solid State Ionics 192 (1) (2011) 58–64.

[57] A.R. Armstrong, C. Lyness, M. Ménétrier, P.G. Bruce, Structural polymorphism in Li_2CoSiO_4 intercalation electrodes: a combined diffraction and NMR study, Chem. Mater. 22 (5) (2010) 1892–1900.

[58] C.A.J. Fisher, N. Kuganathan, M.S. Islam, Defect chemistry and lithium-ion migration in polymorphs of the cathode material Li_2MnSiO_4, J. Mater. Chem. A 1 (13) (2013) 4207–4214.

[59] R. Dominko, D.E. Conte, D. Hanzel, M. Gaberscek, J. Jamnik, Impact of synthesis conditions on the structure and performance of Li_2FeSiO_4, J. Power Sources 178 (2) (2008) 842–847.

[60] R. Chen, R. Heinzmann, S. Mangold, V.S.K. Chakravadhanula, H. Hahn, S. Indris, Structural evolution of $Li_2Fe_{1-y}Mn_ySiO_4$ (y = 0, 0.2, 0.5, 1) cathode materials for Li-ion batteries upon electrochemical cycling, J. Phys. Chem. C 117 (2) (2013) 884–893.

[61] A. Liivat, J. Thomas, J. Guo, Y. Yang, Novel insights into higher capacity from the Li-ion battery cathode material Li2FeSiO4, Electrochim. Acta 223 (2017) 109–114.

[62] C. Deng, S. Zhang, Y. Gao, B. Wu, L. Ma, Y.H. Sun, B.L. Fu, Q. Wu, F.L. Liu, Regeneration and characterization of air-exposed Li_2FeSiO_4, Electrochim. Acta 56 (21) (2011) 7327–7333.

[63] B.O. Mysen, The structural behavior of ferric and ferrous iron in aluminosilicate glass near meta-aluminosilicate joins, Geochim. Cosmochim. Acta 70 (9) (2006) 2337–2353.

[64] E. Uchaker, M. Gu, N. Zhou, Y. Li, C. Wang, G. Cao, Enhanced intercalation dynamics and stability of engineered micro/nano-structured electrode materials: vanadium oxide mesocrystals, Small 9 (22) (2013) 3880–3886.

[65] T. Tachikawa, T. Majima, Metal oxide mesocrystals with tailored structures and properties for energy conversion and storage applications, Npg Asia Mater 6 (2014) e100.

[66] J.R. Hart, Ethylenediaminetetraacetic acid and related chelating Agents, in: Ullmann's Encyclopedia of Industrial Chemistry, 2011.

[67] N.T.K. Thanh, N. Maclean, S. Mahiddine, Mechanisms of nucleation and growth of nanoparticles in solution, Chem. Rev. 114 (15) (2014) 7610–7630.

[68] M. Chirita, R. Banica, A. Ieta, I. Grozescu, Fe-EDTA thermal decomposition, a route to highly crystalline hematite (alpha Fe_2O_3) nanoparticle synthesis, Part. Sci. Technol. 28 (3) (2010) 217–225.

[69] Y. Fujishiro, T. Sato, A. Okuwaki, Homogeneous precipitation of transition metal (Co^{2+}, Fe^{2+}, Ni^{2+} and Zn^{2+}) phosphates under hydrothermal conditions utilizing metal polyaminocarboxylate complex as a precursor, Phosphorus Res. Bullet. 4 (1994) 1–6.

[70] J.J. De Yoreo, P.U.P.A. Gilbert, N.A.J.M. Sommerdijk, R.L. Penn, S. Whitelam, D. Joester, H. Zhang, J.D. Rimer, A. Navrotsky, J.F. Banfield, A.F. Wallace, F.M. Michel, F.C. Meldrum, H. Cölfen, P.M. Dove, Crystallization by particle attachment in synthetic, biogenic, and geologic environments, Science 349 (6247) (2015) aaa6760.

[71] P.W. Voorhees, The theory of Ostwald ripening, J. Stat. Phys. 38 (1) (1985) 231–252.

[72] F. Chen, Q. Gao, G. Hong, J. Ni, Synthesis and characterization of magnetite dodecahedron nanostructure by hydrothermal method, J. Magn. Magn. Mater. 320 (11) (2008) 1775–1780.

[73] Z. Zhu, J. Du, J. Li, Y. Zhang, D. Liu, An EDTA-assisted hydrothermal synthesis of $BiVO_4$ hollow microspheres and their evolution into nanocages, Ceram. Int. 38 (6) (2012) 4827–4834.

[74] M.K. Devaraju, T. Tomai, I. Honma, Supercritical hydrothermal synthesis of rod like Li2FeSiO4 particles for cathode application in lithium ion batteries, Electrochim. Acta 109 (2013) 75–81.

[75] Z. Ding, D. Zhang, Y. Feng, F. Zhang, L. Chen, Y. Du, D.G. Ivey, W. Wei, Tuning anisotropic ion transport in mesocrystalline lithium orthosilicate nanostructures with preferentially exposed facets, Npg Asia Mater 10 (7) (2018) 606–617.

[76] J. Yang, X. Kang, L. Hu, X. Gong, S. Mu, Nanocrystalline-Li_2FeSiO_4 synthesized by carbon frameworks as an advanced cathode material for Li-ion batteries, J. Mater. Chem. A 2 (19) (2014) 6870–6878.

[77] D.P. Lv, J.Y. Bai, P. Zhang, S.Q. Wu, Y.X. Li, W. Wen, Z. Jiang, J.X. Mi, Z.Z. Zhu, Y. Yang, Understanding the high Capacity of Li_2FeSiO_4: in situ XRD/XANES study combined with first-principles calculations, Chem. Mater. 25 (10) (2013) 2014–2020.

[78] A.W. Brownrigg, G. Mountjoy, A.V. Chadwick, M. Alfredsson, W. Bras, J. Billaud, A.R. Armstrong, P.G. Bruce, R. Dominko, E.M. Kelder, In situ Fe K-edge X-ray absorption spectroscopy study during cycling of Li_2FeSiO_4 and $Li_{2.2}Fe_{0.9}SiO_4$ Li ion battery materials, J. Mater. Chem. A 3 (14) (2015) 7314–7322.